# High-fidelity continuum modeling predicts avian voiced sound production

Weili Jiang[a,1], Jeppe H. Rasmussen[b,1,2], Qian Xue[a], Ming Ding[c,d], Xudong Zheng[a,3], and Coen P. H. Elemans[b,3]

[a]Department of Mechanical Engineering, University of Maine, Orono, ME 04469; [b]Department of Biology, University of Southern Denmark, 5230 Odense M, Denmark; [c]Department of Orthopaedic Surgery and Traumatology, Odense University Hospital, 5000 Odense C, Denmark; and [d]Department of Clinical Research, University of Southern Denmark, 5000 Odense C, Denmark

Edited by John G. Hildebrand, University of Arizona, Tucson, AZ, and approved January 22, 2020 (received for review January 7, 2020)

**Voiced sound production is the primary form of acoustic communication in terrestrial vertebrates, particularly birds and mammals, including humans. Developing a causal physics-based model that ultimately links descending vocal motor control to tissue vibration and sound requires embodied approaches that include realistic representations of voice physiology. Here, we first implement and then experimentally test a high-fidelity three-dimensional (3D) continuum model for voiced sound production in birds. Driven by individual-based physiologically quantifiable inputs, combined with noninvasive inverse methods for tissue material parameterization, our model accurately predicts observed key vibratory and acoustic performance traits. These results demonstrate that realistic models lead to accurate predictions and support the continuum model approach as a critical tool toward a causal model of voiced sound production.**

birdsong | human voice | syrinx | larynx | computational fluid dynamics

Of all human vocalizations, the subset of voiced sounds has been most intensively studied (1–4). During voiced sound production, laryngeal vocal folds exhibit self-sustained vibrations through fluid–tissue interactions and elastic restoring forces. These vibrations mechanically convert expiratory airflow into pulsatile airflow, which causes air pressure oscillations constituting the acoustic excitation of the system (1–4). This physical framework is known as the myoelastic-aerodynamic theory (2, 3) and shared between mammals and birds (5). Extensive studies in humans have established that vocal fold posturing, tissue properties, and aerodynamic forces all interact to ultimately control vocal fold kinematics and glottal flow that subsequently set crucial acoustic source parameters such as fundamental frequency, registers, and spectral slope (1–4, 6). However, because of experimental limitations with in vivo human subjects, animal models, excised larynges, and physical models, we still lack systematic experimental data to causally link vocal fold biomechanical properties to phonation (1, 7).

Due to these limitations, computational biophysical models have been instrumental to systematically explore the high-dimensional control space of vocal fold vibration (7–15). In humans, biophysical models range in complexity from reduced-order, lumped-element models that approximate vocal folds as discrete coupled mass-spring-damper systems (16) to high-fidelity continuum models that include the full fluid–structure–acoustics interaction (FSAI) complexity of voiced sound production in anatomically realistic geometries of vocal fold and tract (4, 7–14). While reduced-order models allow broad exploration of simplified control spaces with little computational power (16), they essentially lack physiological representation of tissue properties and geometry (1, 4, 16). High-fidelity continuum models on the other hand are computationally expensive and allow only limited parameter exploration (7–14), but offer realistic representations of voice physiology and can causally link vocal fold biomechanical properties to phonation (7). Additionally, high-fidelity FSAI models allow implementation of muscles that are anatomically correctly placed (15), which is critical to their function (17–19). The high-fidelity continuum model approach is thus a promising tool when realistic representations of voice physiology and biomechanics are essential, such as in the clinical management of voice disorders (1, 4), and ultimately understanding motor control of human (15, 20, 21) or avian (22–25) voiced sound production.

However, the high-fidelity continuum model approach currently faces three key challenges (1, 4). First, the implementation itself of complex high-fidelity FSAI models that include accurate description of physiological parameters and are capable of resolving the large range of spatial and time scales remains challenging (7–14). Second, on the experimental side, although partial physiological datasets have been collected in mammals (1, 2, 20, 21), we currently lack quantification of all critical physiological parameters in single individuals. This would include parameterization of anatomical boundary conditions and vocal fold tissue properties; and time-resolved quantification of flow, pressure, and vocal fold posturing changes due to motor control, and vocal fold shape within single oscillations. Third, because we lack these complete individual-based datasets, FSAI model predictions have not been subjected to thorough experimental validation, essential to strengthen confidence in the continuum model approach in general.

Birds also use voiced sound production to communicate (5), but in contrast to humans, have the major advantage that the entire neuromechanical motor control loop of their voice production, including neural circuitry and vocal organ biomechanics, is experimentally accessible (24, 25). The process of song motor sequence learning in songbirds can be monitored individually

## Significance

**Vocal communication is critical to the reproduction and survival of mammals and birds. Computational physics-based models can facilitate understanding the relation of voice physiology to sound, but there is currently an absence of thorough experimental validation. Here, we present and experimentally test a high-fidelity, continuum model for voiced sound production in birds that includes anatomically realistic geometries of the syrinx and associated vocal tract. We show that, driven by physiologically quantifiable inputs, our model accurately predicts vibration and sound parameters. These data strongly support the continuum model approach as an important component of a causal model of voiced sound production.**

Author contributions: W.J., J.H.R., Q.X., X.Z., and C.P.H.E. designed research; W.J., J.H.R., Q.X., M.D., X.Z., and C.P.H.E. performed research; Q.X., X.Z., and C.P.H.E. contributed new reagents/analytic tools; W.J., J.H.R., Q.X., X.Z., and C.P.H.E. analyzed data; and W.J., J.H.R., Q.X., X.Z., and C.P.H.E. wrote the paper.

The authors declare no competing interest.

This article is a PNAS Direct Submission.



[1]W.J. and J.H.R. contributed equally to this work.

[2]Present address: Department of Marine Biology, Texas A&M University at Galveston, Galveston, TX 77554.

[3]To whom correspondence may be addressed. Email: xudong.zheng@maine.edu or coen@biology.sdu.dk.

This article contains supporting information online at https://www.pnas.org/lookup/suppl/doi:10.1073/pnas.1922147117/-/DCSupplemental.

First published February 13, 2020.

and shares many parallels with human speech acquisition (26–29). Furthermore, we recently developed methodology that allows detailed quantification of sound-producing structures in the excised avian vocal organ under controlled conditions (5). Birds are thus not only a tractable model system for studying the biophysics (5, 22, 24, 25) and learned motor control of voiced sound production (26–29), but also provide unique opportunities to resolve the outstanding challenges for the high-fidelity continuum approach to voiced sound production.

In this study, we implemented a physics-based, high-fidelity three-dimensional (3D) continuum model of voiced sound production in birds and tested this model experimentally with individual-based, physiologically quantifiable inputs. Our high-fidelity model accurately predicted observed key vibratory and acoustic performance traits. Realistic high-fidelity models thus lead to accurate predictions and, as such, support the continuum model approach as a critical tool toward a causal model of voiced sound production.

## Results and Discussion

First, we implemented a 3D immersed-boundary, finite element method-based fluid–structure interaction solver (*SI Appendix*, *Methods and Materials*), where airflow was governed by 3D, unsteady, viscous, incompressible Navier–Stokes equations and dynamics of the avian vocal fold analog were governed by the Navier equation. The fluid and structure solvers were explicitly coupled through a Lagrangian interface where airway and vibrating structures contacted. To allow rapid simulations when resolving the large range of spatial and time scales in simulating voice production, we used the Message Passing Interface parallelization method (30), combined with the immersed-boundary method as an advanced numerical method designed especially for simulating moving boundaries. By carrying out simulations on Cartesian grids, immersed-boundary methods circumvent complicated remeshing algorithms in conventional body-fitted mesh methods and can deal with complex moving boundaries. This approach allows for high-fidelity models that include accurate description of geometries, material properties as well as an accurate solution procedure and strong validation.

To address the second challenge regarding quantification of all critical physiological parameters in single individuals, we focused on rock pigeons, where we previously (5, 31) achieved high-quality kinematic data of the avian vocal fold analog, the lateral vibratory masses (LVMs, Fig. 1*A*). We quantified syringeal anatomy for five individuals using DiceCT scans and implemented high-resolution, finite-element meshes of the syrinx (Fig. 1*A*). To mimic the anatomical



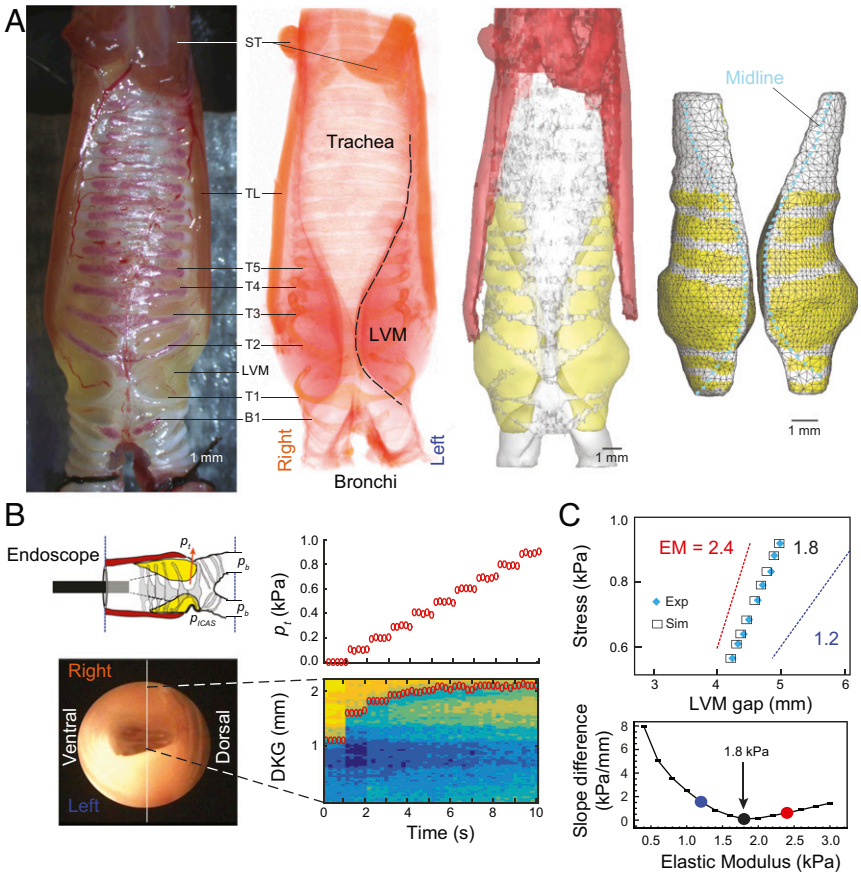


**Fig. 1.** Parameterization of vocal organ geometry and tissue properties. (*A*) Workflow to parameterize FSAI model geometry (Subject P1), with from left to right: (*i*) photo of syrinx mounted in in vitro experimental setup, (*ii*) voltex rendering of iodine contrasted microCT scan showing the bilateral LVM, (*iii*) 3D anatomy, and (*iv*) finite element mesh of LVM solid domain. Yellow and white mesh elements on the LVM outer surface have free and zero displacement boundary conditions, respectively. (*B*) Tissue properties were determined by a combined experimental and modeling approach. A stepwise increase of transmural pressure $p_t$ (*Upper*) caused a stepwise sideways displacement of the LVMs (*Lower*) as viewed by digital kymogram (DKG) along the white vertical line in the endoscopic image (*Left*). (*C*) We used a reverse engineering approach to determine the LVM elastic modulus (EM) for each individual. (*Upper*) Stress-gap width curve of experimental (blue diamonds) and modeled displacement for LVMs with EM = 1.8 kPa (black squares). Also indicated are simulated aligned gap widths of EM = 1.2 (blue line) and 2.4 kPa (red line). (*Lower*) Minimal difference between experimental and simulated data indicates occurs at EM = 1.8 kPa for this individual. B1, bronchial ring; $p_t$, transmural pressure; ST, sternotrachealis muscle; T1–T5, tracheal rings; TL, tracheolateralis muscle.

constraint of the trachea rings on the motion of the LVMs, zero-displacement boundary conditions were applied at mesh nodes where tracheal rings were located. Unilateral LVMs consisted of 1,988–4,620 and 2,159–4,693 nodes and 8,101–18,657 and 9,838–19,131 elements in the solid domain for left and right LVM, respectively (*SI Appendix*, Table S1). To parameterize LVM tissue elasticity in each individual, we developed a noninvasive, combined experimental/simulation approach. We experimentally induced static LVM displacement by stepwise increase of the pressure differential between bronchus and syrinx surrounding air sac, i.e., transmural pressure (Fig. 1*B*). We subsequently used the LVM finite-element model combined with genetic-algorithm–based optimization (32) to simulate LVM displacement as a function of transmural pressure (Fig. 1*C*) and find the elastic modulus value with the smallest difference between experiment and simulation (Fig. 1*C*). These values were used for further dynamic simulation and ranged from 1.8 to 4.0 kPa for the five individuals (*SI Appendix*, Table S1).

To quantify flow, pressure, and LVM posturing changes due to motor control, we applied boundary conditions where LVM vibration was obtained reliably previously (5, 31) to both the experimental preparation and FSAI model ($p_b$ = 1.0 kPa, $p_{icas}$ = 0.5 kPa). Both the in vitro syrinx and corresponding individual FSAI models demonstrated self-sustained stable oscillations in all five cases (Fig. 2 and Movie S1). To quantify the time-resolved LVM shape within oscillations, we took advantage of both the unique coronal view offered by the pigeon syrinx (5) and the lack of a dorso-ventral vibrational component (31) to quantify the time-resolved syringeal or glottal opening as a function of caudo-cranial position, i.e., a coronal glottovibrogram (Fig. 2*C*).

To rigorously test the predictions of the FSAI model during dynamic simulation (the third challenge), we used a blinded procedure where the modeling team (W.J., Q.X., and X.Z.) had access only to geometry, static loading test, and pressure boundary conditions, but was blind to all other data of the experimental procedures (performed by J.H.R. and C.P.H.E.). We compared key vibratory and acoustic predictions by the simulations to the behavior in the experiment. The glottovibrogram allowed for comparing four key parameters describing vibratory kinematics: fundamental frequency of the vibration ($f_o$), the speed of the mucosal wave, peak of the minimal glottal opening, and the open-closed quotient. At group level, all predicted values were not significantly

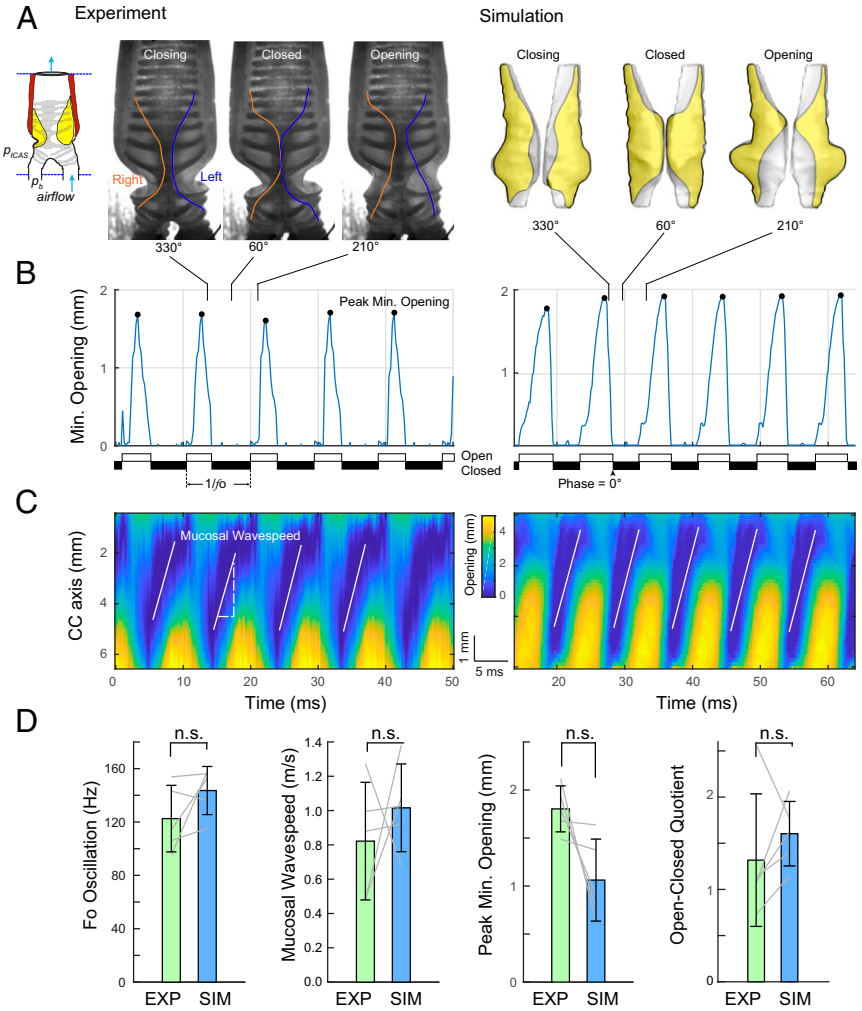


**Fig. 2.** FSAI simulation accurately predicts key features of LVM kinematics. (*A*) Transilluminated syrinx in experiment (EXP, *Left*) and simulation (SIM, *Right*) showing the LVM shape in coronal plane at 330, 60, and 210° of the vibratory cycle, where 0° is defined as the first frame of full closure. (*B*) The minimal glottal opening shows when the glottis in open and closed (white and black horizontal bars) and vibratory frequency $f_o$. The open-closed quotient is the ratio between duration of open and closed glottis. (*C*) Coronal glottovibrogram showing time-resolved glottal opening along caudocranial axis of five oscillations. The white lines indicate the mucosal wave-speed regression slopes based on the closed glottis. (*D*) Observed experimental data and simulation predictions are not significantly different for the above indicated four key kinematic parameters (see *SI Appendix*, Table S2 for values and statistics). n.s., not significant.

different from the experimental values (Fig. 2*D*, for statistics see *SI Appendix*, Table S2). We furthermore compared the time-resolved LVM shape between experiment and simulation at fixed phases within an oscillatory cycle (Fig. 3). During the closed phase (0–120°), the simulated LVM shape matched the experiments very well and was never significantly different from the bootstrapped shape ($P < 0.01$, *SI Appendix*, *Materials and Methods*). The only observed significant ($P > 0.05$, two-sample Kolmogorov–Smirnov test) discrepancy occurred during late closed/early opening in three subjects on one side, where the LVM mass tended to move ∼0.5 mm more cranial (superior in human anatomical terminology) in experiments compared to simulations (Fig. 3 *B* and *C*). Taken together, our FSAI model accurately predicted key kinematic parameters of LVM motion.

Lastly, we compared simulation predictions and experimental observations of two additional key acoustic parameters specifying a sound source—in addition to $f_o$ (Fig. 2*D*)—namely source level and spectral slope, and these did not differ significantly (Fig. 4*A*). Because the simulated LVM vibratory kinematics matched our observations, we used our FSAI models to calculate parameters that could not be quantified in the current experiments, such as spatiotemporal pressure and flow velocity distributions over the vibratory cycle (Fig. 4 *B*–*E*, *SI Appendix*, Fig. S1, and Movie S2). The convergent LVM shape during opening causes high glottal pressures (∼0.9 kPa) that transfer 23.4 ± 15.7 μJ of positive energy ($n = 5$) from flow into LVM (Fig. 4*F*), facilitating opening. When maximum opening is reached at 300° phase, the LVMs are straight (0° angle in Fig. 4*E*), reducing glottal pressure. During early closing, the inferior LVM edge is moving inwards, causing an energy transfer of 7.2 ± 2.2 μJ back into the flow. Consecutively, the LVMs close the glottis by moving together in a divergent shape, causing rapid pressure reduction driven by elastic forces (arrow in Fig. 4*E*). Furthermore, flow inertia in the trachea causes negative pressures (−0.52 ± 0.23 kPa) near the glottis exit prior to full closure (blue region in Fig. 4*D*), facilitating closing. Interestingly, another positive energy transfer to LVMs is observed nearly the end of the cycle. Our avian data thus show that two primary factors contribute to the pressure asymmetry during LVM opening and closing that drive self-sustained oscillation: 1) an alternating convergent/divergent medial surface profile and 2) airflow inertia, corroborating earlier model predictions (33) and measurements on (hemi)larynges (34) in mammalian voice production.

Our FSAI model accurately predicted key performance traits of tissue motion and acoustics driven solely by physiological parameters (static geometry, tissue elasticity, and boundary conditions) and without optimization of either geometry or material properties parameterization on dynamic performance (14). While the FSAI model implementation itself is complex (7–14), the inputs are simple and have, most importantly, directly measurable physiological, material, and geometrical properties. Measurements of vocal fold material properties (35, 36), initial configuration, initial stress, and detailed flow-induced 3D vocal fold motion (37) have been achieved separately in human and mammalian model systems, but complete physiological data sets have not been obtained in these clades, nor in any birds, in single individuals nor consecutively used to thoroughly test FSAI model predictions in a blinded approach. Recent studies encouragingly suggested that realistic continuum 3D models lead to more robust vocal fold dynamics compared to 1D and 2D models (38). Our data shows that realistic continuum 3D models also lead to accurate predictions.

Continuum models currently allow only limited systematic parameters exploration because they are computationally expensive (7). In contrast, phenomenological reduced order models—that simplify mammalian vocal folds or their avian analogs to one or two masses (39, 40)—allow broad exploration of a simplified control space with less computational power and as such have been used widely to capture the dynamics of mammalian (16) and avian voiced sound production (22, 41–43). However, because reduced order models are not first-principle physics models, they



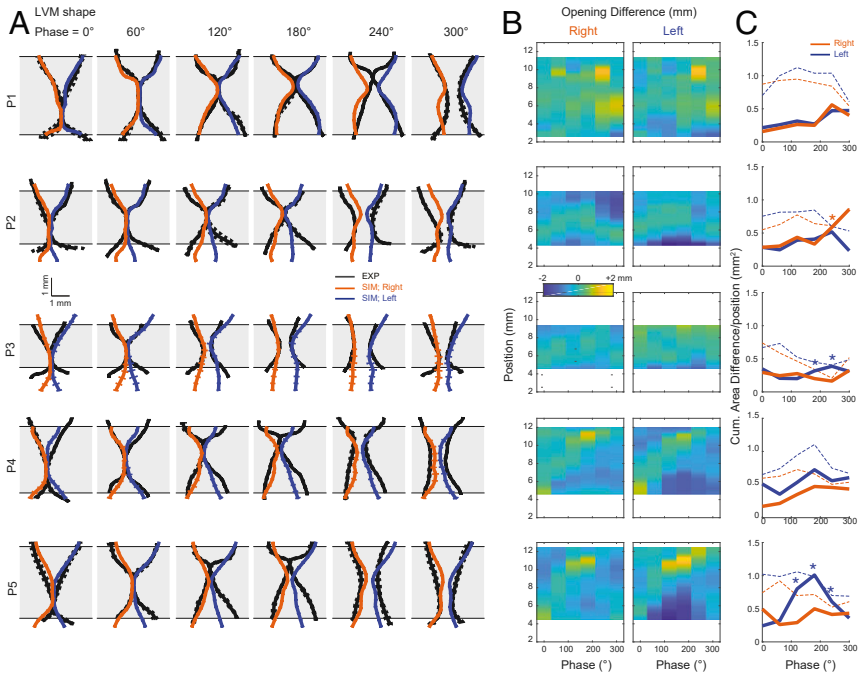


**Fig. 3.** FSAI simulation accurately predicts within-cycle LVM shape. (*A*) Bilateral LVM shape of experiment (EXP) and simulation (SIM) in coronal plane at 0, 60, 120, 180, 240, 300° averaged over five cycles (mean [solid lines] ± SD [dotted lines]). Lateral position difference between experiment and simulation left and right LVMs (*B*) and unsigned cumulative area difference between experiment and simulation (*C*) shows that the predicted shapes are very similar to the observed shapes. The most pronounced discrepancies occur during late closed/early opening. Dotted lines are mean. Asterisks indicate significant difference ($P > 0.01$) between simulation data and 1000x bootstrapped experimental LVM shapes for two-sample Kolmogorov–Smirnov tests.

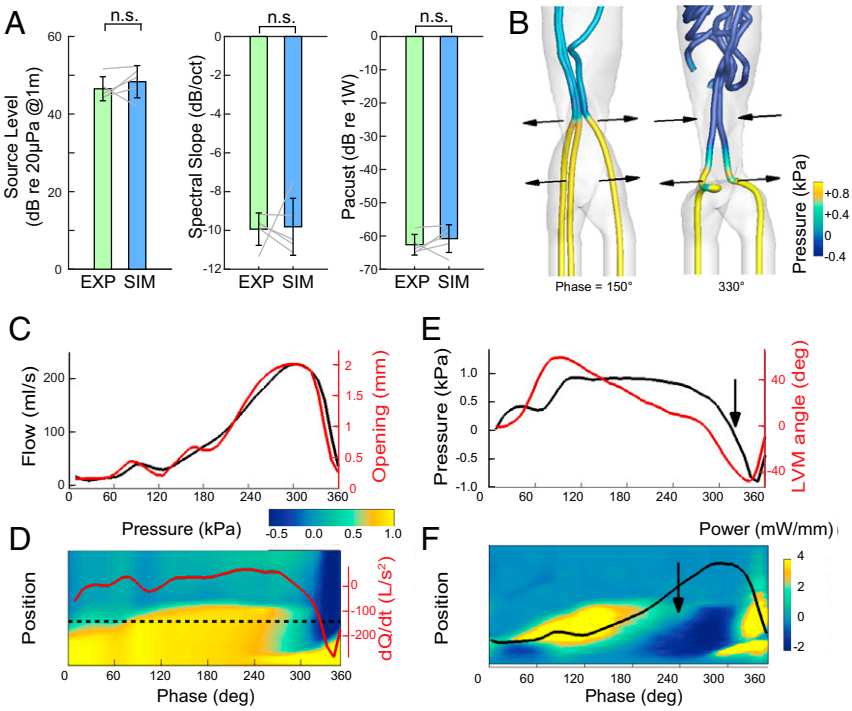


**Fig. 4.** FSAI predictions of acoustics and spatiotemporal pressure and power profiles. (*A*) The simulations accurately predicted key acoustic parameters: source level, spectral slope, and acoustic power. n.s., not significant. (*B*) Three-dimensional flow inside the syrinx as indicated by flow streamlines (pressure color-contoured). Horizontal arrows indicate the motion direction of the LVMs. (*C*) Flow rate Q (black line) correlates strongly with glottal opening (red). (*D*) Spatiotemporal pressure distribution along the airway centerline over a cycle with superimposed dQ/dt (red solid line) as a proxy for sound pressure. (*E*) Glottal pressure (black line) evaluated at the horizontal dotted line in *D* with LVM angle (red line). (*F*) Spatiotemporal power transfer distribution from flow to LVM evaluated along the airway centerline with superimposed flow Q (black solid line).

essentially lack physiological representation of tissue properties and geometry (1, 4, 16). Reducing computational costs and time is thus crucial for making continuum models useful in experimental or clinical settings (1). Rapid developments in machine learning tools combined with supercomputing provide promising avenues to predict complex flow solvers (44, 45) that could significantly reduce computational power and allow elaborate parameter exploration.

In this study, we did not explore or systematically vary parameters that are under neural control. Instead we present strong support for the continuum model approach as a critical first step toward the endeavor of integrating in vitro, ex vivo, and in vivo experimental data with brute force computational approaches into a causal model of motor control of voiced sound production applicable to birds and mammals.

## Methods

We implemented a 3D immersed-boundary, finite-element method-based fluid–structure interaction solver to simulate voice production in the avian syrinx. We quantified individual syringeal anatomy and tissue properties in six adult domestic pigeons (*Columba livia*) and measured the LVM shape, pressure, and acoustic output during sound production in vitro. To eliminate the chance of fitting model predictions on experimental data, we tested the model predictions in a blinded procedure. For a detailed description of the methods, please see *SI Appendix, Methods and Materials*.

**ACKNOWLEDGMENTS.** We thank T. Christensen, S. Jakobsen, P. Martensen, and F. Mortensen for technical support; I. Adam for discussion, and C. Herbst, and J. Rattcliffe for comments on the manuscript. This research was supported by a Janet Waldron Doctoral Research Fellowship, the University of Maine (W.J.), the Danish Research Council, and the NovoNordisk Foundation (C.P.H.E.).

1. Z. Zhang, Mechanics of human voice production and control. *J. Acoust. Soc. Am.* **140**, 2614–2635 (2016).
2. I. R. Titze, *Principles of Voice Production* (National Center for Voice and Speech, Denver, 2000).
3. J. Van Den Berg, Myoelastic-aerodynamic theory of voice production. *J. Speech Hear. Res.* **1**, 227–244 (1958).
4. R. Mittal, B. D. Erath, M. W. Plesniak, Fluid dynamics of human phonation and speech. *Annu. Rev. Fluid Mech.* **45**, 437–467 (2013).
5. C. P. H. Elemans *et al.*, Universal mechanisms of sound production and control in birds and mammals. *Nat. Commun.* **6**, 8978 (2015).
6. E. B. Holmberg, R. E. Hillman, J. S. Perkell, P. C. Guiod, S. L. Goldman, Comparisons among aerodynamic, electroglottographic, and acoustic spectral measures of female voice. *J. Speech Hear. Res.* **38**, 1212–1223 (1995).
7. Z. Zhang, Cause-effect relationship between vocal fold physiology and voice production in a three-dimensional phonation model. *J. Acoust. Soc. Am.* **139**, 1493–1507 (2016).
8. Q. Xue, X. Zheng, R. Mittal, S. Bielamowicz, Subject-specific computational modeling of human phonation. *J. Acoust. Soc. Am.* **135**, 1445–1456 (2014).
9. W. Jiang, X. Zheng, Q. Xue, Computational modeling of fluid-structure-acoustics interaction during voice production. *Front. Bioeng. Biotechnol.* **5**, 7 (2017).
10. X. Zheng, Q. Xue, R. Mittal, S. Beilamowicz, A coupled sharp-interface immersed boundary-finite-element method for flow-structure interaction with application to human phonation. *J. Biomech. Eng.* **132**, 111003 (2010).
11. R. Mittal *et al.*, A versatile sharp interface immersed boundary method for incompressible flows with complex boundaries. *J. Comput. Phys.* **227**, 4825–4852 (2008).
12. F. Alipour, D. A. Berry, I. R. Titze, A finite-element model of vocal-fold vibration. *J. Acoust. Soc. Am.* **108**, 3003–3012 (2000).
13. D.J. Daily, S. L. Thomson, Acoustically-coupled flow-induced vibration of a computational vocal fold model. *Comput. Struct.* **116**, 50–58 (2013)
14. S. Chang *et al.*, Subject-specific computational modeling of evoked rabbit phonation. *J. Biomech. Eng.* **138**, 011005 (2016).
15. E. J. Hunter, I. R. Titze, F. Alipour, A three-dimensional model of vocal fold abduction/adduction. *J. Acoust. Soc. Am.* **115**, 1747–1759 (2004).
16. B. D. Erath *et al.*, A review of lumped-element models of voiced speech. *Speech Commun.* **55**, 667–690 (2013).
17. E. D. Tytell, P. Holmes, A. H. Cohen, Spikes alone do not behavior make: Why neuroscience needs biomechanics. *Curr. Opin. Neurobiol.* **21**, 816–822 (2011).
18. K. Nishikawa *et al.*, Neuromechanics: An integrative approach for understanding motor control. *Integr. Comp. Biol.* **47**, 16–54 (2007).

19. R. Pfeifer, F. Iida, M. Lungarella, Cognition from the bottom up: On biological inspiration, body morphology, and soft materials. *Trends Cogn. Sci.* **18**, 404–413 (2014).
20. D. K. Chhetri *et al*., Effects of asymmetric superior laryngeal nerve stimulation on glottic posture, acoustics, vibration. *Laryngoscope* **123**, 3110–3116 (2013).
21. D. K. Chhetri, J. Neubauer, D. A. Berry, Neuromuscular control of fundamental frequency and glottal posture at phonation onset. *J. Acoust. Soc. Am.* **131**, 1401–1412 (2012).
22. A. Amador, Y. S. Perl, G. B. Mindlin, D. Margoliash, Elemental gesture dynamics are encoded by song premotor cortical neurons. *Nature* **495**, 59–64 (2013).
23. E. P. Kingsley *et al*., Identity and novelty in the avian syrinx. *Proc. Natl. Acad. Sci. U.S.A.* **115**, 10209–10217 (2018).
24. T. Riede, F. Goller, Peripheral mechanisms for vocal production in birds–differences and similarities to human speech and singing. *Brain Lang.* **115**, 69–80 (2010).
25. C. P. H. Elemans, The singer and the song: The neuromechanics of avian sound production. *Curr. Opin. Neurobiol.* **28**, 172–178 (2014).
26. M. S. Brainard, A. J. Doupe, Translating birdsong: Songbirds as a model for basic and applied medical research. *Annu. Rev. Neurosci.* **36**, 489–517 (2013).
27. O. Tchernichovski, P. P. Mitra, T. Lints, F. Nottebohm, Dynamics of the vocal imitation process: How a zebra finch learns its song. *Science* **291**, 2564–2569 (2001).
28. M. A. Long, M. S. Fee, Using temperature to analyse temporal dynamics in the songbird motor pathway. *Nature* **456**, 189–194 (2008).
29. T. S. Okubo, E. L. Mackevicius, H. L. Payne, G. F. Lynch, M. S. Fee, Growth and splitting of neural sequences in songbird vocal development. *Nature* **528**, 352–357 (2015).
30. W. Gropp, E. Lusk, N. Doss, A. Skjellum, A high-performance, portable implementation of the MPI message passing interface standard. *Parallel Comput.* **22**, 789–828 (1996).
31. J. H. Rasmussen, C. T. Herbst, C. P. H. Elemans, Quantifying syringeal dynamics *in vitro* using electroglottography. *J. Exp. Biol.* **221**, jeb172247 (2018).
32. G. Liu *et al*., An image-guided computational approach to inversely determine in vivo material properties and model flow-structure interactions of fish fins. *J. Comput. Phys.* **392**, 578–593 (2019).
33. I. R. Titze, The physics of small-amplitude oscillation of the vocal folds. *J. Acoust. Soc. Am.* **83**, 1536–1552 (1988).
34. F. Alipour, S. Jaiswal, Phonatory characteristics of excised pig, sheep, and cow larynges. *J. Acoust. Soc. Am.* **123**, 4572–4581 (2008).
35. G. R. Dion *et al*., Functional assessment of the ex vivo vocal folds through biomechanical testing: A review. *Mater. Sci. Eng. C* **64**, 444–453 (2016).
36. A. K. Miri, Mechanical characterization of vocal fold tissue: A review study. *J. Voice* **28**, 657–667 (2014).
37. A. M. Vahabzadeh-Hagh, Z. Zhang, D. K. Chhetri, Three-dimensional posture changes of the vocal fold from paired intrinsic laryngeal muscles. *Laryngoscope* **127**, 656–664 (2017).
38. X. Zheng, R. Mittal, Q. Xue, S. Bielamowicz, Direct-numerical simulation of the glottal jet and vocal-fold dynamics in a three-dimensional laryngeal model. *J. Acoust. Soc. Am.* **130**, 404–415 (2011).
39. K. Ishizaka, J. L. Flanagan, Synthesis of voiced sounds from a two-mass model of the vocal cords. *Bell Syst. Tech. J.* **51**, 1233–1268 (1972).
40. B. H. Story, I. R. Titze, Voice simulation with a body-cover model of the vocal folds. *J. Acoust. Soc. Am.* **97**, 1249–1260 (1995).
41. G. B. Mindlin, The physics of birdsong production. *Contemp. Phys.* **54**, 91–96 (2013).
42. R. Zaccarelli, C. P. H. Elemans, W. T. Fitch, H. Herzel, Modelling bird songs: Voice onset, overtones and registers. *Acta Acust. United Acust.* **92**, 741–748 (2006).
43. C. P. H. Elemans, R. Zaccarelli, H. Herzel, Biomechanics and control of vocalization in a non-songbird. *J. R. Soc. Interface* **5**, 691–703 (2008).
44. B. Kim *et al*., Deep fluids: A generative network for parameterized fluid simulations. *Comput. Graph. Forum* **38**, 59–70 (2019).
45. B. N. Hanna, N. T. Dinh, R. W. Youngblood, I. A. Bolotnov, Machine-learning based error prediction approach for coarse-grid Computational Fluid Dynamics (CG-CFD). *Prog. Nucl. Energy* **118**, 103140 (2020).